

Structural, optical and magnetic properties of $\text{MCuSi}_4\text{O}_{10}$ ($\text{M} = \text{Ba}$ and Sr) blue pigments

S. K. Barbar¹ · K. R. Patel¹ · Sudhish Kumar²

Received: 20 July 2016 / Accepted: 27 October 2016 / Published online: 11 November 2016
© Springer Science+Business Media New York 2016

Abstract Inspired by the ancient art work and recent scientific advances in inorganic blue pigments, we have synthesized polycrystalline ceramic samples of barium copper tetrasilicate ($\text{BaCuSi}_4\text{O}_{10}$) and strontium copper tetrasilicate ($\text{SrCuSi}_4\text{O}_{10}$) using solid state reaction route to understand their crystallography, magnetism and optical behaviour. Powder X-ray diffraction patterns confirmed single phase tetragonal crystal structure with space group $P4/ncc$ for both the pigment samples. The unit cell lattice parameters and other structural parameters of these samples were determined using the Rietveld profile refinements of powder diffractograms. Both of these blue pigments show swift optical absorption below 300 nm and considerable absorption in the visible and infrared regions. The obtained values of band gap for $\text{BaCuSi}_4\text{O}_{10}$ and $\text{SrCuSi}_4\text{O}_{10}$ were found to be 3.61 and 3.52 eV respectively. Temperature and field dependent magnetization measurements are suggestive of paramagnetic state at room temperature and superparamagnetic state at low temperatures in both these compounds. The estimated values of effective magnetic moments were found to be 1.833 and 1.91 μ_B for $\text{BaCuSi}_4\text{O}_{10}$ and $\text{SrCuSi}_4\text{O}_{10}$ respectively. Interestingly these obtained values of magnetic moments are very close to the theoretical value of 1.73 μ_B for Cu^{2+} ion.

1 Introduction

The copper containing inorganic pigments with gillespite-structured tetragonal phases of composition $\text{AECuSi}_4\text{O}_{10}$ (where AE is an alkaline earth metal: Ca, Sr, Ba etc.) have attracted considerable interest in the scientific community over the past several decades due to fact that they are environmentally benign, earth abundant and durable materials for the pigment and dye industries. These materials, as the very rare minerals, are effenbergerite ($\text{BaCuSi}_4\text{O}_{10}$), cuprorivaite ($\text{CaCuSi}_4\text{O}_{10}$) and wesselsite ($\text{SrCuSi}_4\text{O}_{10}$). These pigments are also known as low temperature co-fired ceramics (LTCC). Sophisticated use and applications of these synthetic blue pigments have been found in ancient art and technology since $\sim 3600\text{BC}$ in Egypt (Egyptian blue $\text{CaCuSi}_4\text{O}_{10}$) and also in China $\sim 1200\text{BC}$ (Han blue $\text{BaCuSi}_4\text{O}_{10}$). Despite their status as mineralogical curiosities, these compounds have had an importance in modern materials science due to their complex crystal structures and physical properties. The crystal structure of these alkaline earth (AE): $\text{AECuSi}_4\text{O}_{10}$ pigments were originally determined by Pabst from Weissenberg data and were shown to be isostructural with the slightly more common mineral gillespite ($\text{BaFeSi}_4\text{O}_{10}$) with a tetragonal symmetry belonging to the $P4/ncc$ space group. Rapid developments in the user friendly microelectronic industry demands for miniature microwave devices with a high processing speed. Compared with printed resin boards, low-temperature co-fired ceramics (LTCC: inorganic pigments) are superior materials due to their high frequency characteristics, thermal stability and their capacity for integrating passive components [1, 2].

The LTCC substrates have to possess several characteristics, such as low relative permittivity to increase signal speed, low dielectric loss for selectivity, low temperature coefficient of relative permittivity for thermal stability,

✉ S. K. Barbar
barbar_shivkumar@yahoo.co.in

✉ Sudhish Kumar
skphy@mlsu.ac.in

¹ Materials Science Lab, Department of Physics, J.N.V. University, Jodhpur, India

² Magnetism Laboratory, Department of Physics, M.L. Sukhadia University, Udaipur, India

matching coefficient of thermal expansion so that functional materials can be easily attached them and their high thermal conductivity can dissipate heat in effective manner. Large number of materials with low dielectric constant, low dielectric loss and tunable dielectric properties has been developed in last decade [3]. The sintering temperature of the ceramic must be less than the melting point of electrode materials for LTCC applications because high processing temperatures limit their applications in LTCC based devices [4]. The technology of LTCC usually lower than 1000 °C, is used to produce multilayer microelectronic devices made from ceramic substrates. Due to high rates of productivity in the telecommunications industries, the scientific and industrial communities are very much interested in LTCC technology [5–7]. Thorough characterization of new multifunctional materials is the first steps to be carried out before their use. Brief knowledge of crystal structure, optical, electrical and magnetic properties is essential requirements in modern science and technology.

It is worth to mention that oxides are among the most important materials in the field of science and technology. Synthesis of bulk and nanocrystalline single phase oxide materials in various morphologies have been a subject of intense research. Recently, many nanostructured oxides in the series $\text{CaCu}_3\text{Ti}_4\text{O}_{12}$, $\text{ZnFe}_{2-x}\text{LaO}_4$ and $\text{Ce}(\text{MoO}_4)_2$ have attracted considerable research interest due to their complex structural, optical, electrical and magnetic properties [8–10].

Crystal structure and structural properties of the two inorganic blue pigments $\text{BaCuSi}_4\text{O}_{10}$ and $\text{SrCuSi}_4\text{O}_{10}$ have been reported by couple of groups [11, 12]. The crystal structures of solid solution $\text{Sr}_{1-x}\text{Ba}_x\text{CuSi}_4\text{O}_{10}$ were refined from powder neutron time-of-flight, diffraction data [13].

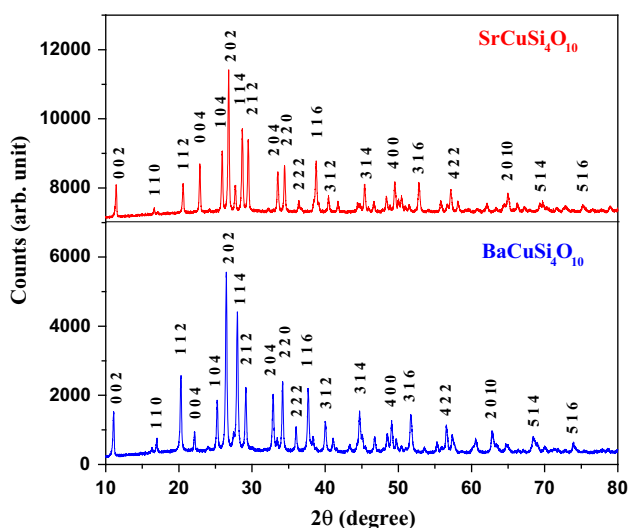


Fig. 1 Room temperature X-ray powder diffractograms of $\text{BaCuSi}_4\text{O}_{10}$ and $\text{SrCuSi}_4\text{O}_{10}$

Theoretical investigation on electronic structures in $\text{BaCuSi}_4\text{O}_{10}$ and $\text{CaCuSi}_4\text{O}_{10}$ were investigated using ligand-field theory (LFT), angular overlap model (AOM) and iterative extended Huckel molecular orbital theory (IET) [14]. A study on microanalysis and crystal structure analysis of blue plate single crystal data have established that these materials belongs to monolayer family in which the structure consists of rings of four linked SiO_4 tetrahedral and each ring is connected to four others to form a silicate layer in the *ab* plane [15].

From the existing literature, it has been observed that number of studies have been carried to synthesize, investigate, analyze and understand the various properties of inorganic pigments, however adequate explanation for the physical properties of these materials is still lacking and demands further improvements. To the best of our knowledge, apart from the existing literature except on glass ceramic and single crystal, there is hardly any reports on the structural refinement using Rietveld analysis, optical and magnetic properties of these materials.

Motivated by the recent scientific advances in exfoliating blue inorganic pigments, in this study we have synthesized two ceramic samples of $\text{BaCuSi}_4\text{O}_{10}$ and $\text{SrCuSi}_4\text{O}_{10}$ using a simple solid state reaction method and carried out detailed studies on their crystal structure, structural refinement, optical and magnetic properties.

2 Experimental details

Two polycrystalline samples in the series of pigments having general formula $\text{MCuSi}_4\text{O}_{10}$ [where M: Ba and Sr, i.e. $\text{BaCuSi}_4\text{O}_{10}$ (effenbergerite) and $\text{SrCuSi}_4\text{O}_{10}$

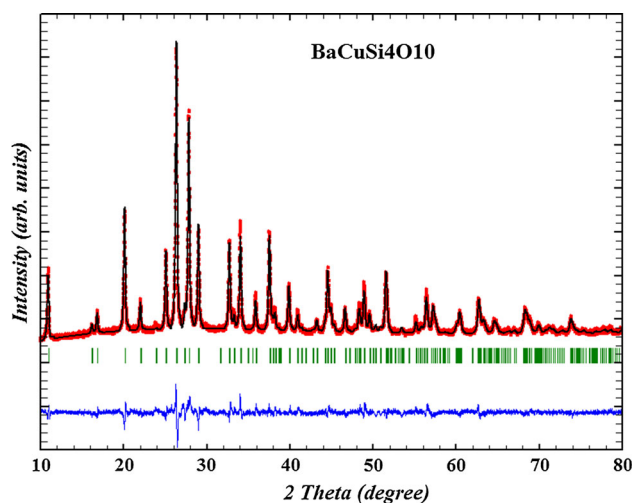


Fig. 2 Refined and fitted X-ray diffraction patterns of $\text{BaCuSi}_4\text{O}_{10}$ at 300 K. Observed (calculated) profiles are shown by *dotted (solid) lines*. The *short vertical marks* represent Bragg reflections. The lower curve is the difference plot

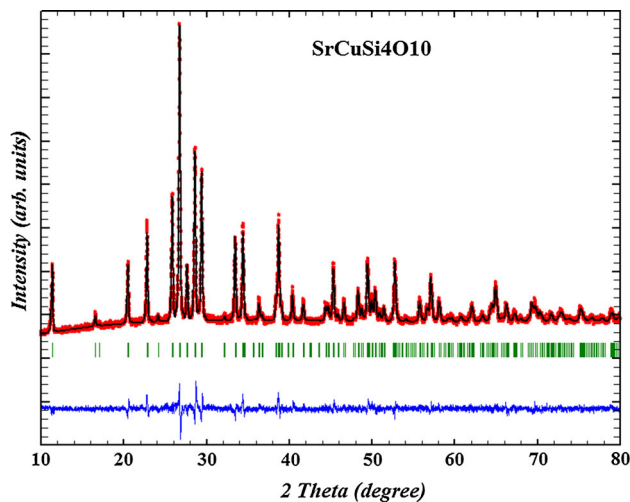


Fig. 3 Refined and fitted X-ray diffraction patterns of $\text{SrCuSi}_4\text{O}_{10}$ at 300 K. Observed (calculated) profiles are shown by dotted (solid) lines. The short vertical marks represent Bragg reflections. The lower curve is the difference plot

(wesselsite)] were synthesized using the solid state reaction route. High purity BaO , SrCO_3 , CuO and SiO_2 powders were thoroughly mixed in the desired stoichiometric proportion in an agate mortar with acetone as the liquid medium for 2 h and then dried in air oven. For obtaining

the homogeneous mixture, the dried mixture was ground to fine powder in an agate mortar for 3 h. Calcinations of the powder samples were done at 1000, 1050 and 1070 °C for 12 and 6 h in a high temperature chamber furnace. The synthesis process was repeated three times in order to reach better homogeneity and full diffusion reaction of the starting material. The resulting mixture was compressed into pellet form by applying pressure using a hydraulic pressure machine. Pellets of both the samples were sintered at 1100 °C for 6 h and then cooled at a rate of 1 °C per minute up to room temperature.

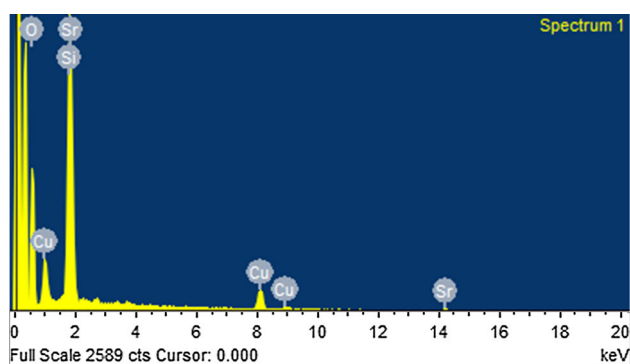
The pellets were crushed to fine powder and the powder products were directly used for the structural and magnetic characterization. The phase purity and quality of the samples were checked by powder X-ray diffractometry (XRD). Powder X-ray diffraction patterns of the two samples were recorded at room temperature on a D-8 Advance X-ray diffractometer with CuK_α radiation ($\lambda = 1.5405 \text{ \AA}$) operated in a step scanning mode at 40 kV and 40 mA. Diffractograms were collected in the 2θ range of 10° – 80° with an increment of 0.02° and 5 s counting time of each step. Detailed structural information such as lattice parameters, atomic positions in the unit cell, profile parameters for pattern, bond distances and reliability factor

Table 1 Summary of refined structural parameters, interatomic distances and atomic positions of atoms for $\text{BaCuSi}_4\text{O}_{10}$ and $\text{SrCuSi}_4\text{O}_{10}$ samples

	Rietveld refined data		Interatomic distances (\AA)						
	$\text{BaCuSi}_4\text{O}_{10}$	$\text{SrCuSi}_4\text{O}_{10}$	$\text{BaCuSi}_4\text{O}_{10}$		$\text{SrCuSi}_4\text{O}_{10}$				
Crystal symmetry	Tetragonal	Tetragonal	Ba–O	2.8958	Sr–O	2.6850			
Space group	P4/ncc	P4/ncc	Cu–Si	3.1936	Cu–Si	3.1803			
$a = b$ (\AA)	7.4421	7.3695	Cu–O	1.9135	Cu–O	1.9187			
c (\AA)	16.1300	15.5811	Si–Si	3.1608	Si–Si	3.1711			
Unit cell volume (\AA^3)	893.353	846.203	Si–O	1.5860	Si–O	1.5994			
Bragg R-factor	6.89	4.95							
R _f -factor	5.77	4.09							
R _p	17.7	18.5							
R _{wp}	16.5	16.9							
GoF	1.6	1.4							
χ^2	2.62	1.94							
Atomic positions									
$\text{BaCuSi}_4\text{O}_{10}$					$\text{SrCuSi}_4\text{O}_{10}$				
Atom	x	y	z	Biso	Atom	x	y	z	Biso
Ba	0.2500	0.7500	0.0000	0.0000	Sr	0.2500	0.7500	0.0000	0.0071
Cu	0.2500	0.2500	0.0949	0.0095	Cu	0.2500	0.2500	0.0885	0.0012
Si	0.5166	0.9390	0.1539	1.2000	Si	0.5082	0.9302	0.1507	1.9600
O1	0.4573	0.9794	0.2570	1.2001	O1	0.4519	0.9811	0.2469	0.0071
O2	0.7242	0.0000	0.1389	0.2000	O2	0.7130	0.0055	0.1310	0.0071
O3	0.3985	0.0401	0.0955	0.3000	O3	0.3697	0.0188	0.0897	0.0071

Table 2 Comparison between observed and calculated interplanar d-spacings

BaCuSi ₄ O ₁₀			SrCuSi ₄ O ₁₀			hkl
2θ	d-obs	d-cal	2θ	d-obs	d-cal	
10.961	8.068	8.065	11.349	7.793	7.791	0 0 2
16.834	5.264	5.262	17.001	5.213	5.211	1 1 0
20.132	4.409	4.407	20.488	4.333	4.331	1 1 2
22.024	4.034	4.032	22.811	3.896	3.895	0 0 4
25.096	3.547	3.545	25.850	3.445	3.444	1 0 4
26.356	3.380	3.379	26.741	3.332	3.331	2 0 2
27.850	3.202	3.201	28.587	3.121	3.120	1 1 4
28.999	3.077	3.076	29.402	3.036	3.035	2 1 2
32.720	2.735	2.735	33.447	2.678	2.677	2 0 4
34.046	2.632	2.631	34.391	2.606	2.605	2 2 0
35.870	2.502	2.501	36.327	2.472	2.471	2 2 2
37.538	2.395	2.394	38.709	2.325	2.324	1 1 6
39.870	2.260	2.259	40.364	2.233	2.233	3 1 2
44.540	2.033	2.033	45.308	2.000	2.000	3 1 4
48.915	1.861	1.860	49.428	1.843	1.842	4 0 0
51.571	1.771	1.771	52.733	1.735	1.734	3 1 6
56.411	1.630	1.630	57.081	1.612	1.612	4 2 2
57.224	1.609	1.608	58.096	1.587	1.586	3 3 4
62.729	1.480	1.480	64.925	1.435	1.435	2 0 10
68.287	1.372	1.372	69.287	1.355	1.355	5 1 4
73.816	1.283	1.283	75.171	1.263	1.263	5 1 6

**Fig. 4** Energy dispersive X-ray (EDX) spectrum of SrCuSi₄O₁₀

were obtained by carrying out Rietveld profile refinements of the diffractograms using the ‘Fullprof’ suite of programs [16]. The ultraviolet visible near infrared (UV–Vis–NIR) absorption spectra in the wave length of 250–1050 nm were recorded using Photodiode Array Spectrophotometer (Specord S600, Analytical Jena). For magnetic characterization, temperature and field dependent magnetization measurements were carried out on a Quantum design SQUID Vibrating Sample Magnetometer (VSM) down to 1.8 K and in field up to 5 T.

3 Results and discussion

3.1 Structural characterization

The XRD patterns of the two samples of BaCuSi₄O₁₀ and SrCuSi₄O₁₀ are shown in Fig. 1. The presence of all the fundamental Bragg reflection belonging to the tetragonal structure (ICSD No. 71864 for BaCuSi₄O₁₀ and ICSD No. 168538 for SrCuSi₄O₁₀) and absence of reflections from any other phase confirm the phase purity and single phase formation of the two synthesized samples.

For obtaining detailed structural information for the two synthesized samples we have carried out Rietveld profile refinements of the XRD patterns in FullProf suite of programs. This technique is based on least square fitting in which the difference between experimental and calculated diffraction patterns is minimized. A good agreement between observed and calculated diffraction data can be found during the refinement, in which number of parameters in the initial model are refined through the least square minimization procedure until the calculated pattern matches the observed profile. The goodness of fit depends on the use of an appropriate starting model and is greatly influenced by the correlation of the parameters which are being refined. In this process, a scale factor, 2θ zero correction, lattice parameters, peak shift, background parameters, profile shape parameters, instrumental parameters, atomic positions, isotropic temperature parameters and occupation numbers can be systematically refined.

The Rietveld profile refinements of these two samples were carried out using tetragonal structure model belonging to the space group P4/ncc. The profile shape has been taken as a Pseudo-Voigt function convoluted with axial divergence symmetry function and a peak asymmetry correction was made for 2θ below 25°. The best fitted XRD patterns of the two samples are presented in Figs. 2 and 3.

The results of the refinements are summarized in Table 1. From the table it is clear that with the substitution of Sr-ion in place of Ba-ion, the lattice parameters decreases which can be explained on the basis of bond length influenced by different factors like ionic radii, valence state, electron affinity. In these two compounds the electron affinity is very high and that is why we observed reduction in the bond distances and hence decrease in the lattice parameters. Moreover, the goodness of fit parameters of the refinements (Bragg R-factor, R_p, R_{wp}, χ^2) were converged to reliable values and indicates for a satisfactory refined model. The refinement also indicate a slight variation in the atomic positions and equivalent isotropic parameters due to the replacement of Ba-atoms by Sr-atoms, which is related to the positions of oxygen atoms while the other atoms kept their fixed position in an unit

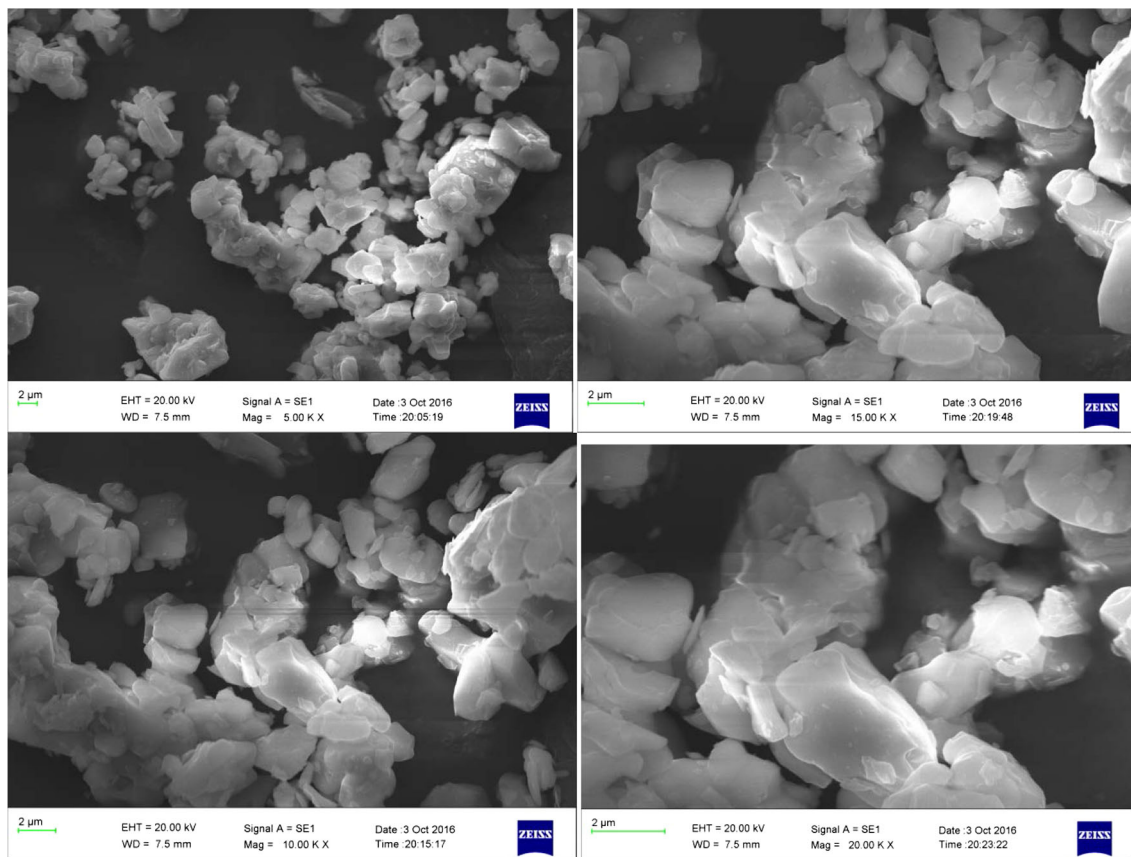


Fig. 5 Scanning electron micrographs (SEM) of the $\text{SrCuSi}_4\text{O}_{10}$

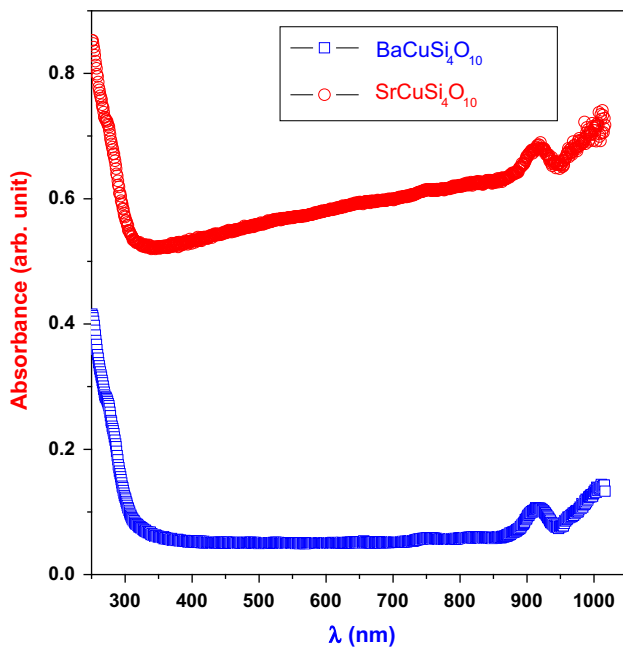


Fig. 6 Optical absorbance spectra of $\text{BaCuSi}_4\text{O}_{10}$ and $\text{SrCuSi}_4\text{O}_{10}$ cell. The major interatomic distances as tabulated in the Table 1 reveals that with the replacement of Sr-atom on Ba-atom site, there is not a big difference in bond lengths

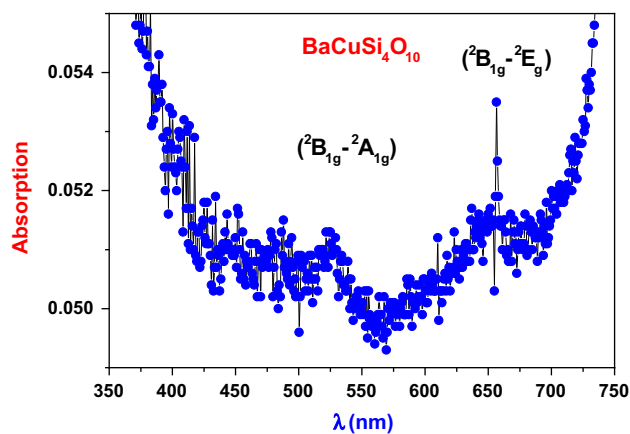
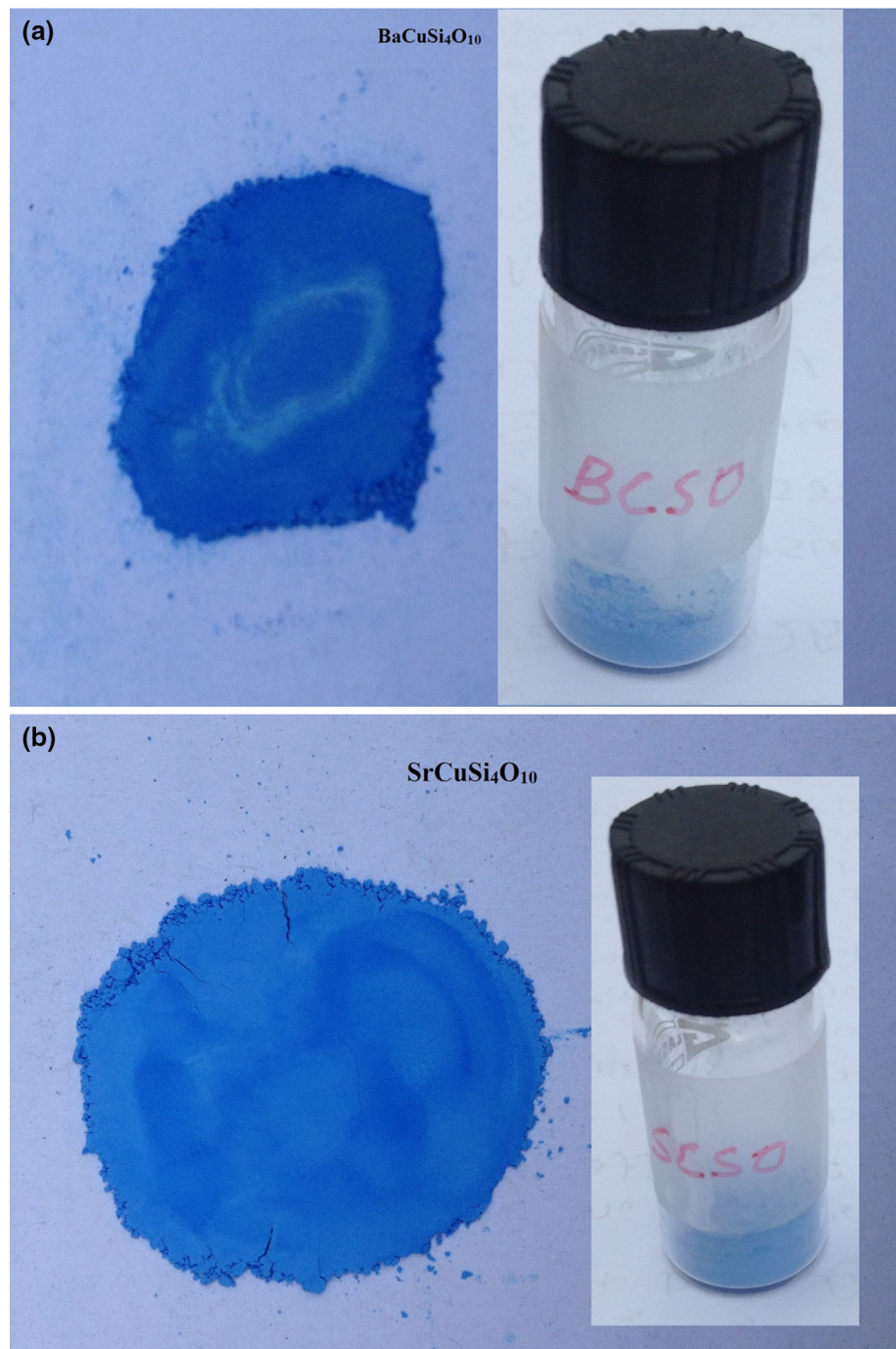


Fig. 7 Optical absorbance spectra of $\text{BaCuSi}_4\text{O}_{10}$ in the visible region

for Cu–Si, Cu–O, Si–Si and Si–O bonds but we can clearly see the change in bond length for bond Sr–O in place of bond Ba–O. A lower bond length for Sr–O can be easily understood on the basis of ionic radii of Sr-ion which is lower than the ionic radii of Ba-ion.

A comparison between observed (obtained from the Bragg's condition i.e. $d = \lambda/2\sin \theta$) and calculated (based on refined parameters) interplanar spacing (d -values) for

Fig. 8 Real image of synthesized powder of
a $\text{BaCuSi}_4\text{O}_{10}$ and
b $\text{SrCuSi}_4\text{O}_{10}$



both the compounds is shown in Table 2. From the table, it can be seen that there is a very little difference ($\leq 0.02 \text{ \AA}$) between d_{obs} and d_{cal} . Thus we have obtained very good agreement between d_{obs} and d_{cal} for both the compounds. From the table it is also observed that with the substitution of Sr on the place of Ba ion, there is a significant change in the d -values. This change in d -values can also be explained in terms of difference in ionic radii of

Sr^{2+} with that of Ba^{2+} ion. As the size of Sr^{2+} ion (1.12 \AA) is smaller than the size of Ba^{2+} (1.35 \AA), the lattice spacing of Sr based compound is smaller than the Ba based compound.

Figure 4 shows the energy dispersive X-ray (EDX) analysis spectrum of $\text{SrCuSi}_4\text{O}_{10}$. The quantitative estimation of the elements obtained directly from the spectrum through its weight and atomic percentages have been found

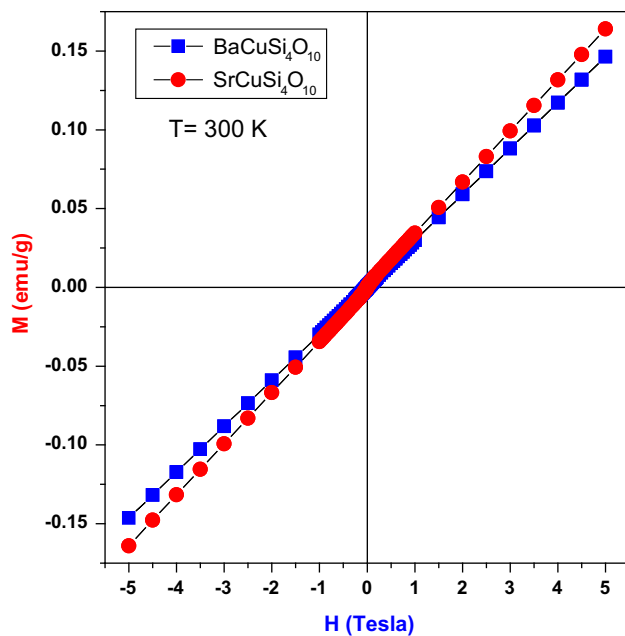


Fig. 9 Magnetization recorded as a function of external magnetic field at 300 K

in very good agreement with the starting materials. These observations further confirmed the stoichiometry of the synthesized $\text{SrCuSi}_4\text{O}_{10}$ sample.

Figure 5 demonstrates scanning electron micrographs (SEM) of the $\text{SrCuSi}_4\text{O}_{10}$ sample. These four SEM images clearly show that the investigated sample essentially consist of some irregular and random shaped grains. The average shape and size of the grains is in micron.

3.2 Optical characterization

Figure 6 illustrates UV–Vis–NIR optical absorbance spectra of the two samples. These spectra clearly shows two characteristic features: swift absorption in the UV range (below 300 nm) and a cusp peaking at ~ 925 nm. Based on these absorption spectra the absorption edge (where the absorbance value is minimum) for $\text{BaCuSi}_4\text{O}_{10}$ and $\text{SrCuSi}_4\text{O}_{10}$ were determined. Using the obtained absorption edge values the band gap energy was calculated. The obtained values of band gap for $\text{BaCuSi}_4\text{O}_{10}$ and $\text{SrCuSi}_4\text{O}_{10}$ were found to be 3.61 and 3.52 eV respectively. These values are in agreement with the literature.

Further in the visible region (Fig. 7) two weak transitions can be easily located, which are originated from the d–d transitions. These transitions occur in the wave length range at ~ 530 nm (green: ${}^2B_{1g} \rightarrow {}^2A_{1g}$) and 650 nm (red: ${}^2B_{1g} \rightarrow {}^2E_g$). These are weakly allowed transitions due to vibrational coupling despite approximate D_{4h} symmetry at copper centre [17]. The two samples absorb weakly but appreciable in the visible region and that is why

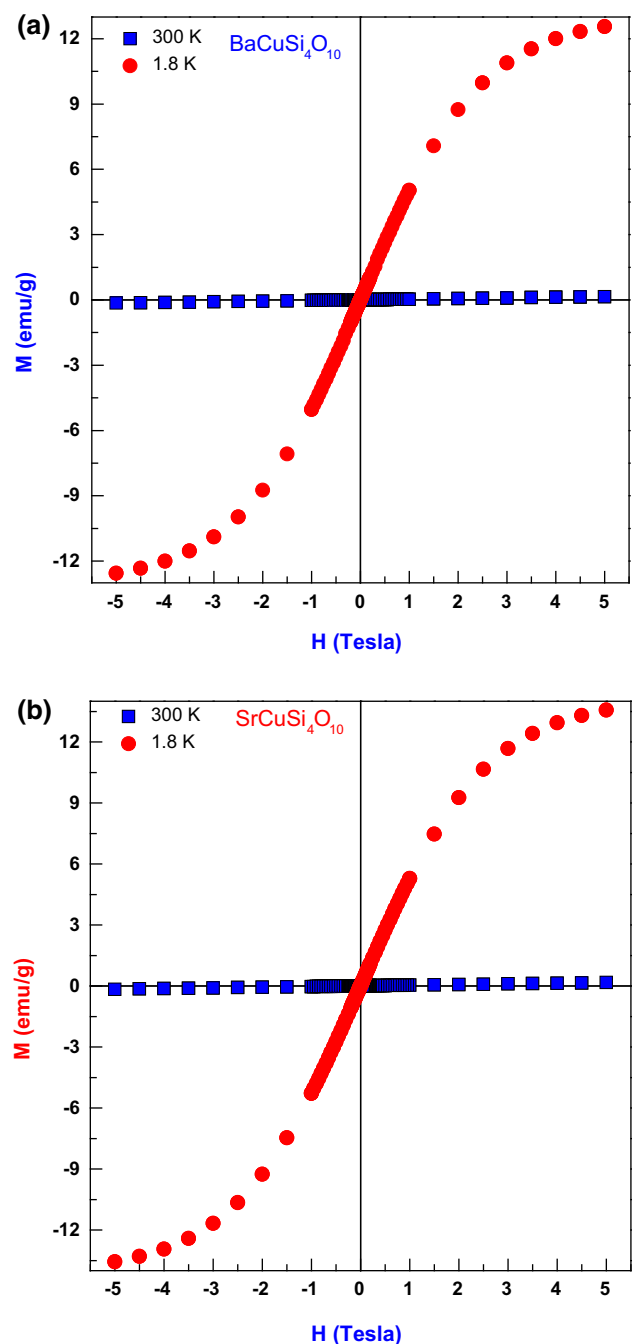


Fig. 10 Magnetic moment recorded as a function of external magnetic field at 1.8 and 300 K. **a** $\text{BaCuSi}_4\text{O}_{10}$ and **b** $\text{SrCuSi}_4\text{O}_{10}$

complementary they display visible blue colour as seen in the Fig. 8a, b.

3.3 Magnetic characterization

Figure 9 displays the variation of the magnetization as a function of the external magnetic field (H) at 300 K for the two pigment samples. The reversible nature of the two M–H curves clearly shows that these two samples are

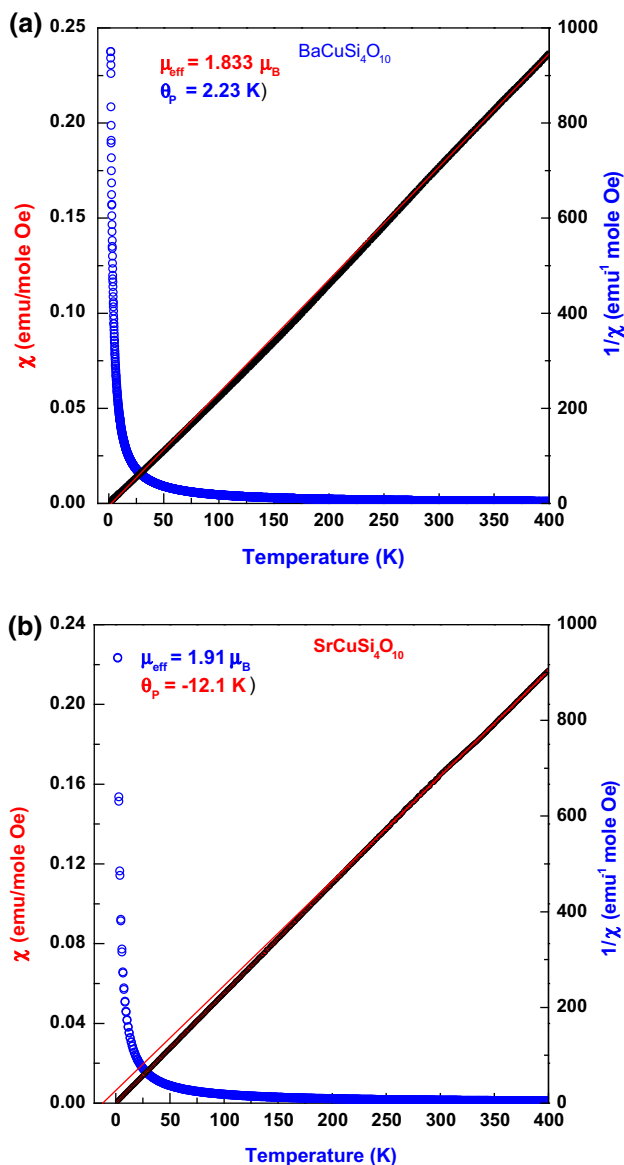


Fig. 11 Magnetic moment, recorded as a function of temperature under an external magnetic field of 1 T **a** BaCuSi₄O₁₀ and **b** SrCuSi₄O₁₀

paramagnetic at room temperature. It is worth to note that the induced magnetization of Sr doped sample is higher than the Ba doped sample.

Figure 10a, b shows the variation of the magnetization as a function of the external magnetic field (H) at 1.8 and 300 K. At 1.8 K in both the samples initially, the magnetization increases rapidly with H but after ~20 kOe the increase becomes quite sluggish. It is worth to note that even at a very high field of 5 T the magnetization does not get saturate, this observation is suggestive of high magnetocrystalline anisotropy in these two samples. Further, at 1.8 K and in an external magnetic field of 50 kOe, the values of the moment are ~12 and ~14 emu g⁻¹ for

BaCuSi₄O₁₀ and SrCuSi₄O₁₀ respectively. However no remanent magnetization and coercivity has been observed in these two samples at 1.8 and 300 K. These observations clearly rule out the long range ferromagnetic ordering in these two samples and suggestive of superparamagnetic state at 1.8 K.

In order to further look for a magnetic transition in these two samples we have carried out temperature dependent magnetization measurements (M–T curves) in an external field of 1 T. Figure 11a, b illustrates the response of magnetization with temperature. Absence of Brillouin type appearance in these two M–T curves clearly rules out a ferromagnetic to a paramagnetic trend in these samples. However, the abrupt change of magnetization at a temperature below ~5 K and the shape of the M–H curve at 1.8 K is suggestive of a superparamagnetic to paramagnetic transition.

The inverse of the paramagnetic susceptibility (χ^{-1}) versus T curve is also plotted in Fig. 11. This inverse susceptibility curve slightly deviates from the Curie–Weiss behaviour and the estimated paramagnetic curie temperature (θ_p) is found to be ~2.2 and –12.1 K for BaCuSi₄O₁₀ and SrCuSi₄O₁₀ respectively. For obtaining the values of effective magnetic moment, the slope of the linear fitted χ^{-1} –T curves were taken and substituted in the following relation: $\mu_{\text{eff}} = 2.828 (\text{slope})^{-1/2}$. Interestingly the estimated values of the effective magnetic moment μ_{eff} are found to be quite high as 1.833 and 1.91 μ_B for BaCuSi₄O₁₀ and SrCuSi₄O₁₀ respectively. These values are very close to the magnetic moment of free Cu²⁺ ions (1.73 μ_B). These observation indicate that randomly dispersed Cu²⁺ ions are responsible for the paramagnetic behavior of the samples at room temperature.

4 Conclusion

In summary, we have synthesized blue pigments of barium copper tetrasilicate (BaCuSi₄O₁₀) and strontium copper tetrasilicate (SrCuSi₄O₁₀) using solid state reaction route. The lattice parameters and other structural parameters of these samples were determined using the Rietveld profile refinements of powder X-ray diffractograms. Both of the pigments show swift optical absorption below 300 nm and considerable absorption in the visible and infrared regions. The obtained values of band gap for BaCuSi₄O₁₀ and SrCuSi₄O₁₀ were found to be 3.61 and 3.52 eV respectively. These two pigments are paramagnetic at room temperature and superparamagnetic at low temperatures. The estimated effective magnetic moment were found to be 1.833 and 1.91 μ_B for BaCuSi₄O₁₀ and SrCuSi₄O₁₀ respectively, which are close to the theoretical value of 1.73 μ_B for Cu²⁺ ion.

Acknowledgements Authors are grateful to Dr. M.S. Roy, Defense Laboratory Jodhpur for providing the UV–Vis–NIR facility and Dr. Ambesh Dixit, IIT, Jodhpur for the EDX and SEM measurements.

References

1. R.R. Tummala, *J. Am. Ceram. Soc.* **74**, 895 (1991)
2. Y. Imanaka, *Multilayered Low Temperature Cofired Ceramics (LTCC) Technology* (Springer, New York, 2005), pp. 1–15
3. M.T. Sebastian, *Dielectric Materials for Wireless Communication* (Elsevier, Oxford, 2008)
4. M.T. Sebastian, H. Jantunen, *Int. Mater. Rev.* **53**, 57 (2008)
5. A. Bittner, A. Ababuneh, H. Seidel, U. Schmid, *Appl. Surf. Sci.* **257**, 1088 (2010)
6. W. Smetana, B. Balluch, G. Stangl, S. Luftl, S. Seidler, *Microelectron. Reliab.* **49**, 592 (2009)
7. Y. Kobayashi, E. Kato, *J. Am. Ceram. Soc.* **77**, 833 (1994)
8. S.M. Hosseinpour-Mashkani, M. Ramezani, A. Sobhani-Nasab, M. Esmaeili-Zare, *J. Mater. Sci. Mater. Electron.* **26**, 6086 (2015)
9. M. Rahimi-Nasrabadi, M. Behpour, A. Sobhani-Nasab, S.M. Hosseinpour-Mashkani, *J. Mater. Sci. Mater. Electron.* **26**, 9776 (2015)
10. A. Sobhani-Nasab, M. Maddahfar, S.M. Hosseinpour-Mashkani, *J. Mol. Liq.* **216**, 1 (2016)
11. A. Pabst, *Acta Crystallogr.* **12**, 733 (1959)
12. B.C. Chakoumakkos, J.A. Fernandez-Baca, L.A. Boatner, *J. Solid State Chem.* **103**, 105 (1993)
13. K.S. Knight, C.M.B. Henderson, S.M. Clark, *Eur. J. Minerol.* **22**, 411 (2010)
14. C. Lin, *Chin. J. Geochem.* **9**, 132 (1990)
15. H.C. Lin, F.C. Liao, S.L. Wang, *Acta Crystallogr.* **C48**, 1297 (1992)
16. J. Rodriguez-Carvajal, *IUCr Newslett.* **26**, 12 (2001)
17. S. Jose, M.L. Reddy, *Dyes Pigments* **98**, 540 (2013)